Cavity quantum electrodynamics with rare-earth ions in solids

Ding, D.

Chapter 4

Multi-dimensional Purcell effects in an ytterbium-doped ring resonator

Rare-earth ions in solids have been put forward as an interesting system for implementing quantum information schemes [59, 60, 61]. The fact that the $4f$ electronic orbits are shielded by the outer filled $5s$ and $5p$ orbits gives the $4f$ states exceptionally long coherence times, typically on the order of milliseconds. Coherence times up to 30 s have been observed with dynamic decoupling techniques [23]. In the past few years, collective effects of ensembles of rare-earth ions have been used as quantum memories for single photons [5, 6] and quantum entanglement of two remote crystals [24] has been experimentally demonstrated. Single rare-earth ions in crystals were detected by a method of upconversion of the excited state population of the $4f$-$4f$ optical transition into ultraviolet fluorescence [25, 9], by a hybrid method including optics and a single electron transistor [7], and by measuring the weak fluorescence from the $4f$-$4f$ transition using high-resolution laser spectroscopy and optical microscopy [8].

Due to the dipole-forbidden nature of the $4f$-$4f$ transitions of the rare-earth ions, the oscillator strength is very small (on the order of 10^{-6}). To overcome this limitation a high-quality-factor (Q) and small-mode-volume (V) (high Q/V) optical cavity can be employed to enhance the light-ion interaction in the framework of cavity quantum electrodynamics (QED). In the weak coupling regime of cavity QED, this effect is well known as the Purcell effect [15] with the associated Purcell factor that quantifies the enhancement of the spontaneous emission (SE) rate of an emitter. To date rare-earth ions have been studied in photonic crystal cavities [26, 27], whispering-gallery mode ring resonators [28], and Fabry-Perot cavities [29, 30, 31]. A rare-earth-ion-doped silicon nitride (Si_3N_4) ring resonator was also studied in Ref. [26], but there

were no cavity QED phenomena observed due to a low Q/V of the particular ring resonator.

In this chapter, we report an enhanced spontaneous emission (SE) rate of trivalent ytterbium ions (Yb^{3+}) in a high-quality-factor (high-Q) silicon nitride (Si_3N_4) ring resonator from 300 K to 5 K. Because of the structure of the ring resonator, not only is the cavity Purcell effect present, but also enhancements from waveguide modes are present. The former effect is spectrally narrowband and becomes appreciable only in the vicinity of the cavity resonance [15], while the latter effect is intrinsically broadband [62, 63, 64]. The long excited state lifetime of the $4f$-$4f$ transition makes thermal depolarization of Yb^{3+} dipoles important [65]. This causes the coupling of the ions to the modes in all polarizations, even though the ions are initially resonantly excited in a well-defined polarization.

We introduce a theoretical model that separates the different contributions to the SE rate into three discrete channels: a 1D enhancement from the slab waveguide, a 2D enhancement from the channel waveguide, and the 3D Purcell effect from the cavity [66]. We refer to these effects as 1D, 2D, and 3D Purcell effects. By measuring the total Purcell factor as a function of temperature and fitting the theoretical model to the experimental data, we shed light on the different contributions to the enhanced SE rate as well as on the depolarization and decoherence of Yb^{3+} in amorphous silicon dioxide (SiO_2) materials.

4.1 Theory

A unified expression of the maximum Purcell factor F^D for a two-level atom in an optical structure with a D-dimensional mode confinement can be written as [66]

$$F^D = \frac{3}{4\pi^{D-1}} \left(\frac{\lambda}{n}\right)^D \frac{Q_D}{V_D}, \tag{4.1}$$

where λ is the wavelength in vacuum, n is the refractive index of the medium where the atom resides, and Q_D and V_D are generalized quality factors and volumes of the modes, respectively.

For $D = 1$ and 2, Q_D are given by [66]

$$Q_1 = n_p n_g / n^2 \text{ and } Q_2 = n_g / n, \tag{4.2}$$

where n_p (n_g) is the effective phase (group) index of the guided mode. The 1D and 2D Purcell effects are spectrally broadband and therefore are not directly influenced by decoherence of the atom provided that the resonance frequency of the atom ω_a is well below the cut-off frequency of the guided modes.

The expression of Q_3 that includes the influence of decoherence on the Purcell effect is given by [16]

$$Q_3 = \frac{\omega_c \gamma_{\rm tot}/2}{\gamma_{\rm tot}^2 + \Delta^2}, \tag{4.3}$$

where ω_c is the frequency of the cavity resonance, $\Delta = \omega_a - \omega_c$ is atom-cavity detuning, and $\gamma_{\rm tot}$ is the total decoherence rate of the atom-cavity system, given by

$$\gamma_{\rm tot} = \kappa/2 + \gamma/2 + \gamma^*. \tag{4.4}$$

Here $\kappa = \omega/Q_c$ is the cavity field decay rate with Q_c being the cavity quality factor, γ is the atom relaxation rate, and γ^* is a pure dephasing rate. In writing Eqs. (4.3) and (4.4), we have assumed that decoherence of the atom can be modelled as pure dephasing. We note that this assumption may not be valid in some cases, e.g., for a quantum dot coupled to a photonic crystal cavity as in Refs. [67, 68].

The generalized mode volumes V_D are given by

$$V_D = \frac{\int_D \epsilon(\boldsymbol{r})|\boldsymbol{E}(\boldsymbol{r})|^2 \, {\rm d}^D\boldsymbol{r}}{\epsilon(\boldsymbol{r}_{\rm m})|\boldsymbol{E}(\boldsymbol{r}_{\rm m})|^2}, \tag{4.5}$$

where $\epsilon(\boldsymbol{r})$ and $\boldsymbol{E}(\boldsymbol{r})$ are the permittivity and electric field at position $\boldsymbol{r}$, respectively, and $\boldsymbol{r}_{\rm m}$ is an optimal position of the atom where the electric field energy density $\epsilon(\boldsymbol{r})|\boldsymbol{E}(\boldsymbol{r})|^2/2$ is maximized.

The maximum Purcell factor given by Eq. (4.1) only occurs when the atom is located at the optimal position $\boldsymbol{r}_{\rm m}$ and when the dipole of the atom is aligned with the local electric field $\boldsymbol{E}(\boldsymbol{r}_m)$. In a general situation, when these conditions are not satisfied, the actual Purcell factor $F_{\rm r}^D$ is reduced from the maximum value F^D given by

$$F_{\rm r}^D = F^D f(\boldsymbol{r}_0)|\cos\vartheta|, \tag{4.6}$$

where $\boldsymbol{r}_0$ is the actual position of the atom, and ϑ is the angle between the dipole of the atom and the local electric field $\boldsymbol{E}(\boldsymbol{r}_0)$. The spatial function $f(\boldsymbol{r}_0)$ contains the normalized energy density and is expressed by

$$f(\boldsymbol{r}_0) = \frac{\epsilon(\boldsymbol{r}_0)|\boldsymbol{E}(\boldsymbol{r}_0)|^2}{\epsilon(\boldsymbol{r}_{\rm m})|\boldsymbol{E}(\boldsymbol{r}_{\rm m})|^2}. \tag{4.7}$$

For a structure with 1D, 2D, and 3D Purcell effects and with modes polarized along the x-, y-, and z-directions, the total Purcell factor F is a sum of contributions over all the dimensions and modes [66]:

$$F = \sum_{D=1}^{3} \sum_{i,j,k} \Big[F_i^{D,x} f_i^{D,x}(\boldsymbol{r}_0)|\cos\vartheta_x| + F_j^{D,y} f_j^{D,y}(\boldsymbol{r}_0)|\cos\vartheta_y| + F_k^{D,z} f_k^{D,z}(\boldsymbol{r}_0)|\cos\vartheta_z| \Big], \tag{4.8}$$

where $F_i^{D,x}$ is the maximum Purcell factor for the i-th order mode in D-dimension, polarized along the x-direction, $f_i^{D,x}(\boldsymbol{r}_0)$ is the corresponding spatial function, and ϑ_x is the angle of the atomic dipole with respect to the x-direction.

Decoherence processes also depolarize the dipole of the atom during the atom-mode coupling [65] and therefore indirectly influence the 1D, 2D, and 3D Purcell effects. We introduce a degree of polarization Θ ($0 \leq \Theta \leq 1$) to quantify the degree to which the atom maintains its initial dipole direction during its lifetime. $\Theta = 1$ means the dipole of the atom maintains its initial direction, while $\Theta = 0$ means the dipole direction becomes completely random. Without loss of generality, we assume that the dipole is initially aligned with the y-direction. With the dipole depolarization effect, the value of $|\cos\vartheta_y|$ is reduced from one to $(1 + 2\Theta)/3$, while the values of $|\cos\vartheta_x|$ and $|\cos\vartheta_z|$ increase from zero to $(1 - \Theta)/3$. Eventually Eq. (4.8) reads

$$F = \sum_{D=1}^{3} \sum_{i,j,k} \Big[F_i^{D,x} f_i^{D,x}(\boldsymbol{r}_0)(1-\Theta) + F_j^{D,y} f_j^{D,y}(\boldsymbol{r}_0)(1+2\Theta) + F_k^{D,z} f_k^{D,z}(\boldsymbol{r}_0)(1-\Theta) \Big] /3. \tag{4.9}$$

The SE rate of the atom with the Purcell enhancement is

$$k = k_{\mathrm{R}} + k_{\mathrm{NR}} + k_{\mathrm{R}} F, \tag{4.10}$$

where k_{R} is radiative decay rate in free space and k_{NR} is non-radiative decay rate.

4.2 Device

We investigate the Purcell effect in a ring resonator with a radius of 1.59 mm made of a rectangular waveguide that consists of a Si_3N_4 core embedded in SiO_2 cladding [45, 1, 47, 69]. Schematics of the top view of the device and the cross section of the ring resonator are depicted in Figs. 4.1(a) and 4.1(b). The ring resonator is coupled to two straight waveguides via evanescent fields of waveguide modes. Yb ions are implanted into the device and are approximately Gaussian distributed in depth with a full width at half maximum of 86 nm and with a center 72 nm above the Si_3N_4 core top surface. The peak doping concentration is 0.001% (atom number) and is laterally uniform across the device. The device is completed by wafer bonding at 950°C for 3 hours, which anneals defects in the SiO_2 created in the ion implantation process [49]. A single-mode fiber coupled to one of the straight waveguides serves as an input port, while three multimode fibers are coupled to the remaining output ports.

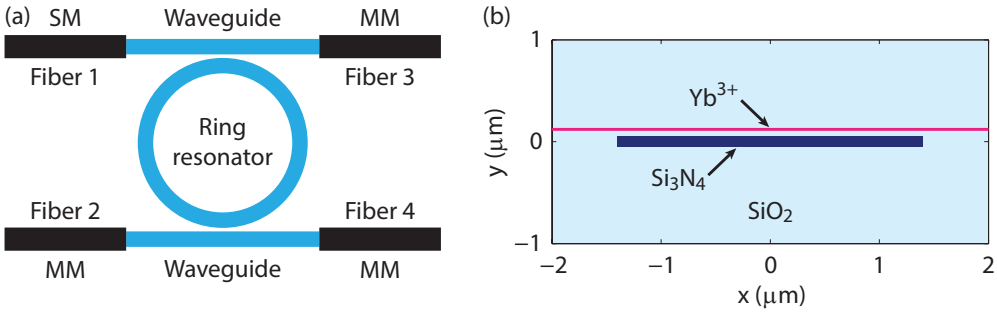

Figure 4.1: (a) Schematic top view of a ring resonator coupled to two straight waveguides and subsequently to four optical fibers. The radius of the ring resonator is 1.59 mm and the coupling gap is 1.8 μm. Fiber 1 is single-mode (SM) and fibers 2–4 are multimode (MM). (b) Schematic cross section of the ring resonator consisting of a Si_3N_4 core embedded in SiO_2 cladding with Yb^{3+} implanted above the core annotated by a red line. The Si_3N_4 core has a width of 2.8 μm and a thickness of 0.1 μm.

We focus on the optical transition of Yb^{3+} centered at 976 nm (vacuum wavelength), which involves the lowest manifold of the ground state ($^2F_{7/2}$) and the lowest manifold of the excited state ($^2F_{5/2}$). The inhomogeneous linewidth of Yb^{3+} caused by different local environments in the host glass matrices is about 1 THz [70] and only weakly depends on temperature T. The homogeneous linewidth Γ_H is largely determined by interactions with phonons and tunnelling systems [71, 72], and therefore is strongly temperature dependent. $\Gamma_H(T)$ for phosphate glass is approximately proportional to $T^{1.8}$ above 40 K and to $T^{1.3}$ below 40 K, with $\Gamma_H(1) \approx 16$ MHz at 1 K [73]. In our device, Yb^{3+} are implanted in amorphous SiO_2 and therefore we expect deviations of these values for $\Gamma_H(T)$.

Around 976 nm, the ring resonator supports three transverse electric (TE) modes and two transverse magnetic (TM) modes as calculated by the finite element method. These mode profiles are shown in Figs. 4.2(a)-4.2(e), corresponding to the 2D modes and cross sections of the 3D modes. The 1D modes are calculated for an infinite Si_3N_4 slab sandwiched in SiO_2 cladding resulting in two 1D modes and their profiles are shown in Figs. 4.2(f) and 4.2(g). The electric fields of the TE (TM) modes are approximately linearly polarized along the $x(y)$-direction. Because of the high-aspect-ratio geometry of the Si_3N_4 waveguide core, the ring resonator is single-mode along the core thickness direction (y-direction) and multimode along the core width direction (x-direction).

The optical properties of the ring resonator at 976.0 nm are first characterized at room temperature by using standard frequency scanning methods. A tunable narrow-linewidth laser is tuned to a central wavelength of 976.0 nm and its frequency is scanned over 70 GHz around the central frequency. The

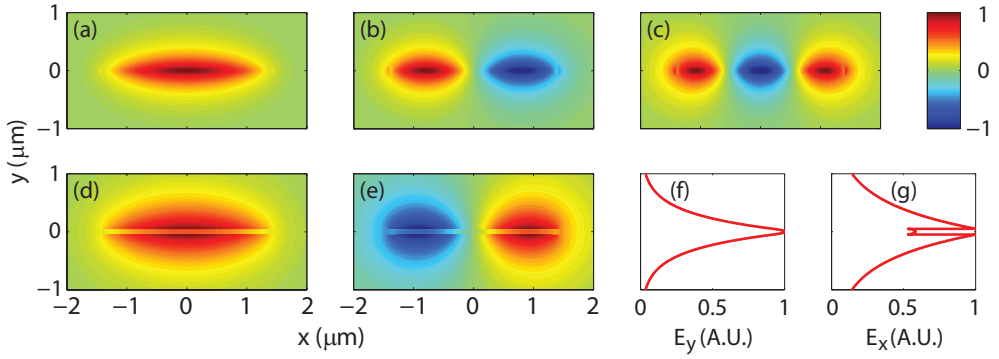

Figure 4.2: Calculated mode profiles of (a) TE_0, (b) TE_1, (c) TE_2, (d) TM_0, and (e) TM_1 at 976 nm for the waveguide as shown in Fig. 4.1(b). The color plots in (a)-(c) represent the x-component of the electric field E_x, while in (d) and (e) they represent the y-component of the electric field E_y. Calculated mode profiles of (f) TE_0 and (g) TM_0 at 976 nm for a slab waveguide with a 0.1 μm thick Si_3N_4 layer in the xz-plane sandwiched in SiO_2 cladding.

output of the laser is coupled to fiber 1 through a fiber polarization controller (FPC). This excites clockwise travelling modes in the ring resonator and these modes are coupled to another straight waveguide and subsequently coupled to fiber 2. The measured transmission through fiber 2 as a function of laser frequency detuning is shown in Fig. 4.3(a). By changing the polarization of the light coupled to the ring resonator using the FPC, the coupling to individual resonances can be optimized and their polarizations can be identified. These polarizations are annotated in Fig. 4.3(a). From the measured data we find free spectral ranges (FSRs) of 19.28, 19.30, and 17.54 GHz corresponding to group indices of 1.557, 1.556, and 1.712 for the TM_0, TM_1, and TE_0 modes, respectively. The corresponding quality factors of these resonances are 4.8×10^6, 5.1×10^5, and 8.3×10^5 that are determined by Lorenztian fits as shown in Figs. 4.3(b)–4.3(d), respectively. We identify these resonances with corresponding modes according to the measured polarizations, FSRs, and quality factors. Resonances of higher order modes are not observed in the frequency scanning measurement because of their relatively low quality factors.

Figure 4.3(e) shows the measured fluorescence spectrum of Yb^{3+} emitted from the ring resonator at room temperature. The laser frequency is tuned to 920.0 nm and is on resonance with the TM_1 mode, which excites Yb^{3+} to the highest manifold of the excited state ($^2F_{5/2}$). The fluorescence is collected by fiber 4 and analyzed by a spectrometer through a long-wavelength-pass filter with a cutoff wavelength of 950 nm. The broad peak centered at 976 nm is a characteristic feature of Yb^{3+} corresponding to the transition from the lowest manifold of the excited state to the lowest manifold of the ground state.

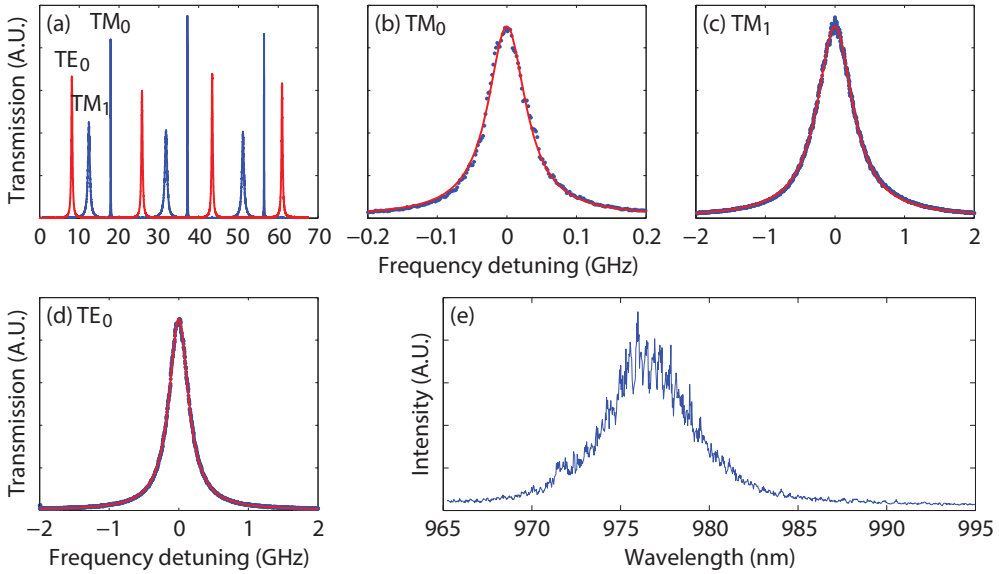

Figure 4.3: (a) Laser transmission around 976.0 nm as a function of frequency detuning. Transmission is measured through fiber 2 while the frequency of the laser coupled to fiber 1 is scanned over 70 GHz. The laser polarization is either set along the y-direction (blue curve) or the x-direction (red curve). The observed resonances are assigned to the corresponding modes according to their polarizations, quality factors, and free spectral ranges. Detail of the measured resonances (blue dots) of the (b) TM_0, (c) TM_1, and (d) TE_0 modes, together with fits to a Lorentzian lineshape (red curves). The quality factors derived from the fits are 4.8×10^6, 5.1×10^5, and 8.3×10^5, respectively. (e) Measured fluorescence spectrum of Yb^{3+} emitted from the ring resonator at room temperature. The broad peak centered at 976 nm is a characteristic feature of Yb^{3+} corresponding to the transition from the lowest manifold of the excited state ($^2F_{5/2}$) to the lowest manifold of the ground state ($^2F_{7/2}$).

4.3 Experiment and results

A schematic of the setup used to measure the SE rate of Yb^{3+} is shown in Fig. 4.4. The fiber-coupled device is mounted in a helium bath cryostat. The output of a narrow-linewidth (100 kHz) laser at 976.0 nm is chopped by a mechanical chopper and coupled into a fiber beamsplitter (FBS). The resulting pulse has an "on" ("off") time of 1 (9) ms and a measured rise and fall time less than 0.5 μs. One of the outputs of the FBS is used as a trigger signal. Another output of the FBS is coupled to fiber 1 through a fiber polarization controller (FPC). The FPC is set to maximize the transmission of the resonance of TM_0 measured at fiber 2. The laser frequency is locked to the resonance of TM_0 by using frequency modulation techniques [74]. The output of fiber 4 is used to measure the SE of Yb^{3+} by a single photon counting module (SPCM) through

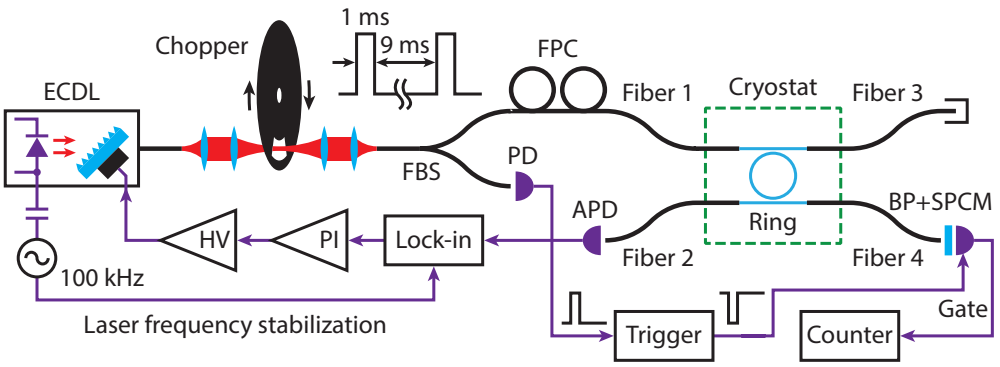

Figure 4.4: (a) Schematic of the setup used to measure spontaneous emission (SE) rate of Yb^{3+} in a ring resonator. Abbreviations: external cavity diode laser (ECDL), fiber beam splitter (FBS), fiber polarization controller (FPC), Yb^{3+}-doped ring resonator (Ring), photodetector (PD), avalanche photodetector (APD), bandpass filter (BP), single photon counting module (SPCM), lock-in amplifier (Lock-in), proportional-integral controller (PI), high-voltage amplifier (HV). Black curves denote optical fibers and purple lines denote electrical wirings.

a bandpass filter ($\lambda_0 = 976$ nm, $\Delta\lambda = 2$ nm). The SPCM is gated off (on) when the laser pulse is on (off) by the trigger signal. When the laser pulse is on, the output power in fiber 2 is about 1 nW. This low pumping level ensures that heating effects in the ring resonator are negligible. The SE events of the Yb^{3+} ensemble are counted starting after the falling edge of the laser pulse with time bins of 0.5 μs.

Two decay curves measured at 295 K and 5.7 K are shown in Fig. 4.5. They both contain components with varying Purcell factors and decay rates due to the spatial and spectral distributions of Yb^{3+}. The fastest decay rate for the data at 5.7 K is clearly larger than that at 295 K. We are interested in the maximum Purcell factor F_m in our system for the ions located at $x = 0$ in Fig. 4.1(b). To estimate the value of F_m by using Eq. (4.8), we first approximate the implantation depth distribution $u(y)$ as an average position y_0 using the calculated mode profiles of the 1D modes $\boldsymbol{E}(y)$:

$$y_0^i = \frac{\int \epsilon(y)|\boldsymbol{E}^i(y)|^2\, u(y) y\, \mathrm{d}y}{\int \epsilon(y)|\boldsymbol{E}^i(y)|^2\, u(y)\, \mathrm{d}y},\ i = \mathrm{TM}_0 \text{ or } \mathrm{TE}_0, \tag{4.11}$$

where $\epsilon(y)$ and $\boldsymbol{E}^i(y)$ are $\epsilon(\boldsymbol{r})$ and $\boldsymbol{E}^i(\boldsymbol{r})$ at $x = z = 0$. Because of the high aspect-ratio of the Si_3N_4 core, the normalized electric field distributions $\boldsymbol{E}^i(y)$ are approximately the same for the modes with the same polarizations in all dimensions. This approximation is valid because the effective index method is a good approximation to calculate the modes of the waveguide with a high aspect-ratio and compares well with the FEM simulation [69]. In the

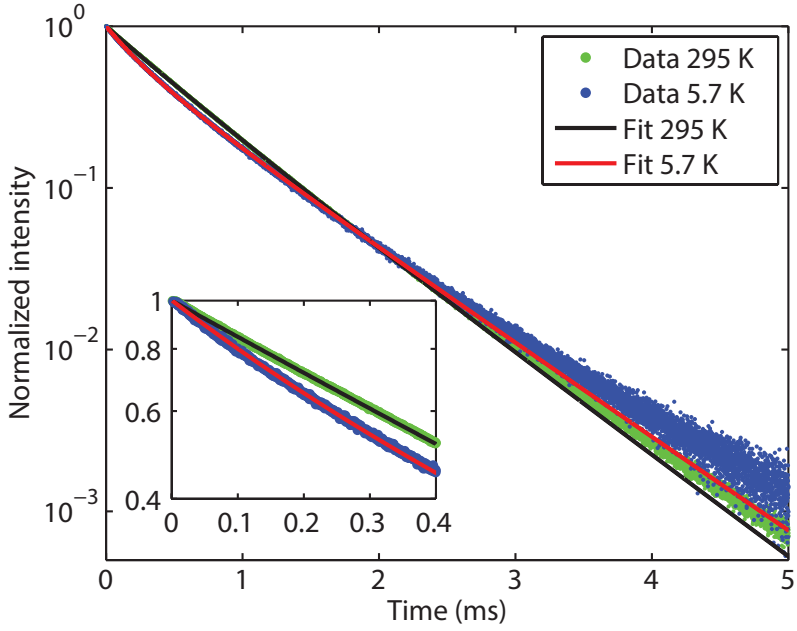

Figure 4.5: Measured spontaneous emission (SE) decay data at 295 K (green dots) and 5.7 K (blue dots) in a logarithmic scale with time bins of 0.5 μs and the fits (black and red curves) to a decay function. The data are obtained by averaging over 5×10^5 single decay traces. The dark counts are subtracted and the maximum counts are normalized to unity. The absolute maximum counts of the data at 5.7 K is lower than that at 295 K, because less ions spectrally overlap with the laser at 5.7 K. Inset: magnified main graph in the initial 0.4 ms.

effective index method, the confinement in the vertical direction is calculated independently of the horizontal direction. Since the waveguide is single-mode in the vertical direction, the normalized electric field distributions $\boldsymbol{E}^i(y)$ are approximately identical for all the modes, and only depends on the polarization.

We neglect the Purcell effects of higher order modes because of their larger V_D and smaller Q_D as compared to the fundamental modes. With these approximations, we obtain

$$\begin{aligned} F_{\mathrm{m}} =& (F_p^1 + F_p^2 + F_p^3) f_p(y_0^p)(1 + 2\Theta)/3 \\ &+ (2F_q^1 + F_q^2 + F_q^3) f_q(y_0^q)(1 - \Theta)/3, \end{aligned} \tag{4.12}$$

where $p \equiv \mathrm{TM}_0$, $q \equiv \mathrm{TE}_0$, and the polarizations of the modes denoted by the superscript of $F_i^{D,x}$ in Eq. (4.8) are included in p and q. Simulation of Eq. (4.12) shows that the Purcell factor from a single mode dominates in most of temperature ranges. This enables us to approximate this dominant single-mode profile along the Yb^{3+} sheet ($y = y_0^i$ and $z = 0$, $i = \mathrm{TM}_0$ or TE_0) as

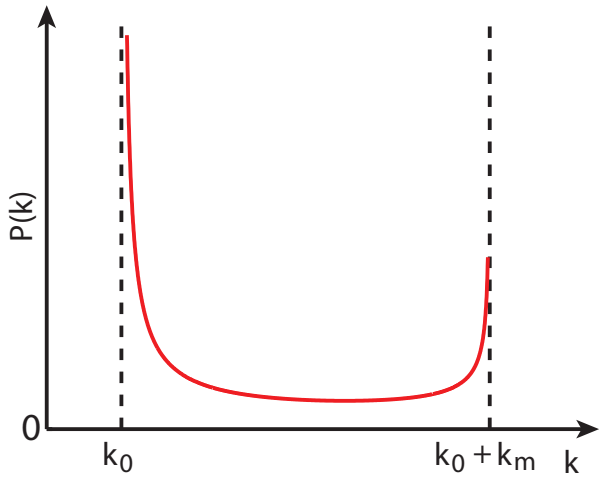

Figure 4.6: Probability density function $P(k)$ as a function of decay rate k. $P(k)$ approaches infinity at free-space spontaneous emission (SE) rate k_0 and at $k_0 + k_\mathrm{m}$ with k_m being the maximum enhanced SE rate.

a Gaussian function $h(x)$ at a specific temperature. Hence the Purcell factor $F(x)$ for the ions located at position x can be written as

$$F(x) = h(x)F_\mathrm{m}, \text{ with } h(0) = 1. \tag{4.13}$$

The position-dependent decay rate $k(x)$ is then readily available as

$$k(x) = k_\mathrm{R} + k_\mathrm{NR} + h(x)k_\mathrm{R}F_\mathrm{m} \equiv k_0 + h(x)k_\mathrm{m}, \tag{4.14}$$

where k_R is free-space radiative decay rate, k_NR is non-radiative decay rate, k_0 is free-space SE rate, and k_m is the maximum enhanced SE rate.

The probability density of Yb^{3+} decaying with a rate k is proportional to the number of ions $\mathrm{d}N$ in an infinitesimal interval $\mathrm{d}k$ around k:

$$P(k) \propto \left|\frac{\mathrm{d}N}{\mathrm{d}k}\right| = 2\rho\left|\frac{\mathrm{d}x}{\mathrm{d}k}\right|_{x>0} = 2\rho\left|\frac{\mathrm{d}k}{\mathrm{d}x}\right|^{-1}_{x>0}, \tag{4.15}$$

where ρ is a linear doping density of Yb^{3+} and we have used a monotonic part of $h(x)$ to derive $P(k)$. By using a Gaussian function of $h(x)$, we obtain

$$P(k) = \begin{cases} \dfrac{A/(k-k_0)}{\sqrt{\ln k_\mathrm{m} - \ln(k-k_0)}} & k_0 < k < k_0 + k_\mathrm{m}, \\ 0 & k \le k_0,\ k \ge k_0 + k_\mathrm{m}, \end{cases} \tag{4.16}$$

where A is a normalization factor rendering $\int P(k)\,\mathrm{d}k = 1$. Figure 4.6 shows the property of $P(k)$ with $P(k)$ approaching infinity at k_0 and $k_0 + k_\mathrm{m}$. A

decay function $I(t)$ can be built as $I(t) = \int P(k) \exp(-kt)\, \mathrm{d}k$ with $I(0) = 1$. We note that the more generally applied method of analyzing decay data using a double-exponential function is only a crude approximation in our system compared to the decay function $I(t)$ built from $P(k)$. Besides, the double-exponential function has one more fitting parameter compared to our decay function $I(t)$, which unnecessarily complicates the interpretation of the result.

From fitting the measured SE decay curve at a given temperature with $I(t)$, we obtain the values of k_0 and k_m. Examples at 295 K and 5.7 K are shown in Fig. 4.5 with extracted values of $k_0 = 1.41$ and 1.30 (± 0.01) ms^{-1}, and $k_\mathrm{m} = 1.2$ and 4.6 (± 0.2) ms^{-1}, respectively. Figure 4.7(a) shows k_0 at different temperatures. Due to the large transition energy of Yb^{3+}, multi-phonon transitions are negligible and energy transfer among adjacent ions is the dominant non-radiative decay mechanism [75]. The energy transfer rate k_ET takes the form of [75]

$$k_\mathrm{ET}(T) = B \exp(-\beta/T), \tag{4.17}$$

where B and β are parameters. β is related to the activation energy involved in the energy transfer process. The model $k_0 = k_\mathrm{R} + k_\mathrm{ET}$ is fitted to the data as shown in Fig. 4.7(a) resulting in $k_\mathrm{R} = 1.30 \pm 0.01$ ms^{-1}, $B = 0.13 \pm 0.01$ ms^{-1}, and $\beta = 56 \pm 6$ K.

The measured F_m is obtained as $F_\mathrm{m} = k_\mathrm{m}/k_\mathrm{R}$ and is shown as a function of temperature in Fig. 4.7(b). To model the results by using Eq. (4.12), we assume the average polarization of the ions $\Theta = \exp(-T/\alpha)$ with α being a depolarization parameter. We adopt γ^* from the homogeneous linewidth data of Yb^{3+}-doped phosphate glass [73] except $\Gamma_\mathrm{H}(1)$ as an adjustable parameter. The values of κ are derived from the measured Q_c of the 3D modes. All the other parameters regarding the properties of the ring resonator are obtained through numerical simulations. We set $\Delta = 0$ for the 3D TM_0 mode because of the resonant excitation and $\Delta = 5.0$ GHz for the 3D TE_0 mode. α and $\Gamma_\mathrm{H}(1)$ are the only adjustable parameters in the model. The fit of Eq. (4.12) is shown in Fig. 4.7(b) with $\alpha = 5.3 \pm 0.5$ K and $\Gamma_\mathrm{H}(1) = 5.0 \pm 0.3$ MHz which is smaller than the value in Ref. [73] (16 MHz) for phosphate glass. Contributions from the 1D, 2D, and 3D Purcell effects are shown separately in Fig. 4.7(b). The 1D and 2D Purcell factors are constants at the high temperature limit with $\Theta \approx 0$, while they approach the value for TM_0 when $T \ll \alpha$ ($\Theta \approx 1$). The 3D Purcell factor is small at high temperature where $\Gamma_\mathrm{H}(T)$ is much larger than the linewidth of the cavity resonance, while it increases rapidly when the former becomes comparable with the latter with decreasing temperature. A larger Purcell factor measured at 3 K than at 300 K in Er-doped photonic crystal cavities were reported [26]. For the current system the model predicts F_m to reach about 9 at very low temperature, where the 3D Purcell effect is dominant and is almost only limited by κ of the 3D TM_0 mode.

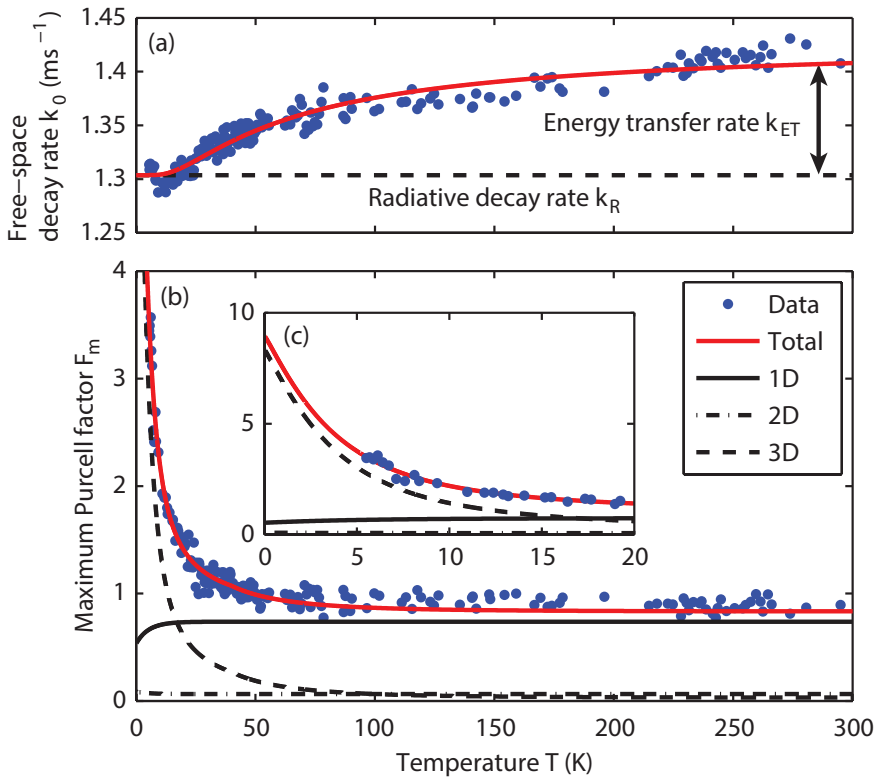

Figure 4.7: (a) Measured free-space decay rate k_0 (blue dots) and the fit (red curve) using the model assuming a constant radiative decay rate k_{R} (dashed line) and a temperature-dependent non-radiative decay rate k_{ET} due to energy transfer among adjacent ions. (b) Measured maximum Purcell factor F_{m} (blue dots) and the fit (red curve) using the model based on the multi-dimensional Purcell effects and the dipole depolarization. The 1D (black solid), 2D (black dashed-dotted), and 3D (black dashed) components are shown. (c) Same physical quantities as in (b) in the range of 0–20 K.

In conclusion, we have introduced a novel solid-state cavity QED system based on high-Q Si_3N_4 ring resonators with implanted rare-earth ions. We have separated one-, two-, and three-dimensional contributions to the Purcell effect and analyzed their temperature dependences. This provides novel insight into the temperature dependence of the depolarization and decoherence of the rare-earth ions. Furthermore, the results indicate that a fully optimized ring resonator with a higher Q/V and an operation temperature below about 100 mK will lead to a much larger Purcell enhancement and eventually enable the optical detection and quantum state control within the $4f$ manifolds of individual rare-earth ions.